The Journal of the Acoustical Society of America

FEBRUARY 02 2026

Transarctic acoustic transmissions during the coordinated Arctic acoustic thermometry experiment in 2019–2020[a]

Matthew A. Dzieciuch ; Hanne Sagen ; Peter F. Worcester ; Espen Storheim ; F. Hunter Akins ; Stein Sandven ; John A. Colosi ; John N. Kemp; Geir Martin Leinebø

J. Acoust. Soc. Am. 159, 1071–1085 (2026)
https://doi.org/10.1121/10.0042233

JASA ARTICLE

Transarctic acoustic transmissions during the coordinated Arctic acoustic thermometry experiment in 2019–2020[a)]

Matthew A. Dzieciuch,[1] Hanne Sagen,[2] Peter F. Worcester,[1,b)] Espen Storheim,[2] F. Hunter Akins,[1] Stein Sandven,[2] John A. Colosi,[3] John N. Kemp,[3] and Geir Martin Leinebø[4]

[1]*Scripps Institution of Oceanography, University of California San Diego, La Jolla, California 92093, USA*

[2]*Nansen Environmental and Remote Sensing Center, N-5007 Bergen, Norway*

[3]*Woods Hole Oceanographic Institution, Woods Hole, Massachusetts 02543, USA*

[4]*Norwegian Coast Guard, 8400 Sortland, Norway*

ABSTRACT:

Acoustic signals with a center frequency of 35 Hz and a full bandwidth of about 4 Hz were transmitted over various ranges along a path extending from north of Svalbard to north of Alaska during the 2019–2020 US-Norwegian Coordinated Arctic Acoustic Thermometry Experiment (CAATEX). Three moorings were installed in the Canada Basin and three in the Nansen Basin, with one mooring in each basin hosting a source. All moorings had vertical receiving arrays, enabling spatial separation of the low-order acoustic normal modes. The modal group delays varied significantly over the year but were roughly consistent with predictions for the decade 2015–2022 based on the World Ocean Atlas 2023. The CAATEX signals traversed nearly the same trans-Arctic acoustic path as the 19.6-Hz signals in the 1994 Transarctic Acoustic Propagation (TAP) experiment. The TAP and CAATEX group delays cannot be directly compared because of the differing carrier frequencies. Thus, an indirect method using the group delays computed using WOA 2023 as a convenient standard was employed, but the large TAP mode-2 travel-time uncertainty precluded definitive comparisons. Nonetheless, CAATEX demonstrated that long-range acoustic transmissions provide precise, year-round measurements of large-scale ocean sound-speed (temperature) variability under the ice.

 https://doi.org/10.1121/10.0042233

(Received 1 September 2025; revised 17 December 2025; accepted 22 December 2025; published online 2 February 2026)

[Editor: Megan S. Ballard] Pages: 1071–1085

I. INTRODUCTION

The Arctic has changed dramatically in recent decades in response to the changing climate caused by increasing concentrations of greenhouse gases. Atmospheric surface temperatures in the Arctic have increased severalfold (e.g., Rantanen *et al.*, 2022), ice extent and thickness have decreased (e.g., Meier and Stroeve, 2022), and the ocean stratification has changed (e.g., Polyakov *et al.*, 2012; Timmermans *et al.*, 2014; Polyakov *et al.*, 2020). Large-scale, continuous observations of the ocean interior for studying and monitoring climate variability are needed but difficult to obtain in ice-covered regions such as the Arctic Ocean. Acoustic signals can travel under the ice, however, and acoustic methods therefore have a special role to play in making measurements in these regions (e.g., APL-UW, 2008; Mikhalevsky *et al.*, 2015; Howe *et al.*, 2019). The 2019–2020 US-Norwegian Coordinated Arctic Acoustic Thermometry Experiment (CAATEX) made measurements of broadband acoustic transmissions at various ranges along a path extending from north of Svalbard in the eastern Arctic to north of Alaska in the Beaufort Sea to quantify gyre and basin-scale temperature variability in the Arctic Ocean. Six moorings were installed in CAATEX: three in the Canada Basin and three in the Nansen Basin. One mooring in each basin had an acoustic source that transmitted signals with a center frequency of 35.0 Hz and a full bandwidth of about 4 Hz. All moorings had long vertical receiving arrays, enabling the spatial separation of the low-order acoustic normal modes. The acoustic impulse responses and year-long time series of the modal group delays (travel times) are presented here for long-range acoustic paths in the western Arctic, eastern Arctic, and across the entire Arctic Ocean. The group delays of some of the modes varied significantly across the signal bandwidth due to waveguide dispersion. The group delay at the center frequency of the signal (35 Hz) and a parameter characterizing the dispersion were therefore jointly estimated (Akins *et al.*, 2025).

The CAATEX mooring locations were chosen such that the acoustic signals traversed nearly the same acoustic path as the signals in the Transarctic Acoustic Propagation (TAP) experiment conducted in April 1994 (Mikhalevsky *et al.*, 1995; Mikhalevsky *et al.*, 1999). During TAP, broadband signals with a center frequency of 19.6 Hz were transmitted from a source at an ice camp north of Svalbard (TURPAN)

[a)]This paper is part of a special issue on Climate Change: How the Sound of the Planet Reflects the Health of the Planet.

[b)]Email: pworcester@ucsd.edu

https://doi.org/10.1121/10.0042233

to receiving arrays at an ice camp approximately 2637 km distant in the Beaufort Sea (SIMI, Sea Ice Mechanics Initiative) to determine the feasibility of using long-range ocean acoustic thermometry to measure basin-scale Arctic Ocean temperatures. TAP reported travel times of acoustic normal mode 2, which primarily sampled the Atlantic Water, that were significantly shorter than computed from the Arctic Ocean climatology available at the time, suggesting that a basin-scale warming of the Atlantic Water had already occurred. Subsequently, in April 1999 as part of the US–Russian Arctic Climate Observations using Underwater Sound (ACOUS) project, broadband signals with a center frequency of 20.5 Hz were transmitted along a nearby acoustic path from a source moored at the northern edge of Franz Victoria Strait to a vertical receiving array at an ice camp approximately 2720 km distant in the Chukchi Sea (Mikhalevsky and Gavrilov, 2001; Mikhalevsky *et al.*, 2001; Gavrilov and Mikhalevsky, 2002, 2006). Mode 2 travel times measured during ACOUS suggested that the Atlantic Water had warmed further. One of the goals of CAATEX was to compare present-day basin-scale heat content with the TAP measurements made on nearly the same trans-Arctic acoustic path in the 1990s. However, the center frequency of the CAATEX transmissions (35 Hz) was significantly higher than that of the TAP and ACOUS transmissions. The expectation was that the reduction in ice thickness (and therefore presumably roughness) in the intervening years would reduce scattering losses and enable trans-Arctic ranges at a higher frequency. Because the vertical structures of the normal modes at 35 Hz differ from those at 19.6 Hz, the travel times of the same mode number at the differing frequencies used in TAP and CAATEX cannot be directly compared, as the sensitivities of the group velocities to the vertical sound-speed structure are not the same. The CAATEX and TAP modal travel times are therefore compared here with predictions made using sound-speed fields computed for decadal time spans from the temperature and salinity fields in the World Ocean Atlas 2023 (WOA 2023) (Locarnini *et al.*, 2024; Reagan *et al.*, 2024a; Reagan *et al.*, 2024b), rather than directly with one another. WOA 2023 is not the truth, of course, given the sparsity of the hydrographic data in the Arctic Ocean, which only gets worse in earlier decades, but WOA 2023 nonetheless provides a convenient standard for comparing the results of the two experiments. The modal group delays measured during CAATEX in fact provide a stringent test of the accuracy of the WOA 2023 fields along the acoustic paths. The application of inverse methods to obtain range-averaged ocean sound-speed (temperature) using the modal group delays between the CAATEX moorings is left for a subsequent paper.

Section II describes the 2019–2020 CAATEX experiment and presents examples of the acoustic data from the vertical receiving arrays. Section III provides data on the oceanographic environment on the CAATEX acoustic path using data obtained during the experiment. Section IV describes how time series of modal group delays (travel times) were generated for the low-order acoustic normal modes. Section V compares the measured travel times in CAATEX and TAP with predictions based on WOA 2023. Some concluding remarks are made in Section VI.

II. THE 2019–2020 CAATEX EXPERIMENT

The 2019–2020 CAATEX experiment is described in the following sections, including the geometry (Sec. II A) and signal processing (Sec. II B).

A. Geometry

Three moorings were deployed in the western Arctic Ocean by the Scripps Institution of Oceanography (SIO1, SIO2, and SIO3), and three moorings were deployed in the eastern Arctic by the Nansen Environmental and Remote Sensing Center (NERSC1, NERSC2, and NERSC3) (Fig. 1 and Table I). The NERSC moorings in the eastern Arctic were originally intended to be distributed from near the North Pole to the location of the TAP acoustic source north of Svalbard, but a combination of difficult ice conditions and a Russian missile exercise conducted at the North Pole with little advance notice prevented more northerly deployments than those shown in Fig. 1. The SIO moorings were deployed between 3 September and 14 October 2019 on the *USCGC Healy*, and the NERSC moorings were deployed between 14 August and 9 September 2019 on the Norwegian Coast Guard ice breaker *KV Svalbard*. All moorings were recovered on the *KV Svalbard*, with the NERSC mooring recoveries occurring between 17 July and

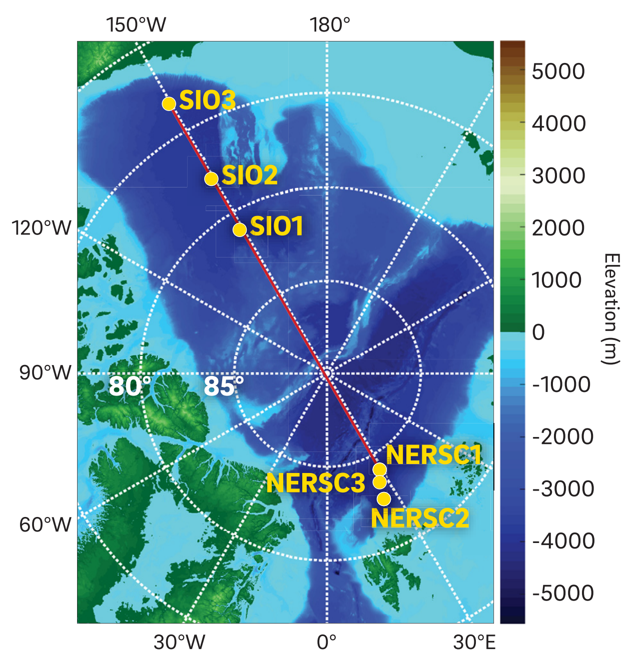

FIG. 1. Geometry of the CAATEX experiment. Broadband 35-Hz acoustic sources were moored at SIO1 and NERSC1. All moorings had vertical receiving arrays. The acoustic path from NERSC1 to SIO3 is shown in red (World Geodetic System 1984, WGS84). The 1994 TAP experiment source (TURPAN) and receiver (SIMI) ice camp locations were close to the positions of NERSC3 and SIO3, respectively. The bathymetry is from the International Bathymetric Chart of the Arctic Ocean Version 5.0 (IBCAO V5.0) (Jakobsson *et al.*, 2024).

TABLE I. Mooring motion reference locations, median source depths, and water depths. Water depths are true depths determined from acoustic surveys of the acoustic release locations, which were 3.25 m above the seafloor.

	Location	Source Depth (m)	Water Depth (m)
SIO1	80.86968°N, 148.34339°W	54	3813
SIO2	77.73014°N, 149.14288°W		3821
SIO3	73.01797°N, 149.57762°W		3735
NERSC1	84.00327°N, 28.39160°E	60	4018
NERSC2	82.51248°N, 23.96282°E		4067
NERSC3	83.44196°N, 25.66723°E		4021

10 August 2020 and the SIO mooring recoveries between 12 October and 25 November 2020. The ranges between the moorings varied from approximately 71 to 2566 km (Table II).

1. Acoustic transceiver moorings

Moorings SIO1 and NERSC1 had GeoSpectrum Technologies Inc. (GTI) C-BASS M72–1000 very low frequency electrodynamic acoustic sources with resonant frequencies of about 35 Hz at a depth of 60 m (GeoSpectrum Technologies Inc., Dartmouth, Nova Scotia, Canada). The source dimensions are small compared to a wavelength at 35 Hz, and the sources are therefore essentially omnidirectional. The maximum root mean square (rms) source level is 195 dB re 1 μPa at 1 m, but reduced source levels were used in CAATEX, as described in the following. The median source depths (as proxies for the source depths when the moorings were vertical) were 54 m for SIO1 and 60 m for NERSC1 (Table I). Each source transmitted once every three days. The transmissions from SIO1 and NERSC1 were separated by 36 h, with SIO1 transmission times beginning on year day 1 at 1200 UTC and NERSC1 transmission times beginning on year day 3 at 0000 UTC, where year day 1 is 1 January 2019. Each source began transmitting shortly after it was deployed. The source controllers were programmed to cease transmissions after 31 October 2020.

Each transceiver mooring had a distributed vertical line array (DVLA) receiver immediately below the sources (Worcester *et al.*, 2009; Worcester *et al.*, 2013). The DVLA on SIO1 had 40 Hydrophone Modules spaced 30.0 m apart, giving an overall aperture of 1170 m. The NERSC1 mooring had 25 Hydrophone Modules spaced 40.0 m apart, giving an overall aperture of 960 m. The DVLA arrays had four-sided hairy fairing overbraid to reduce mooring strum. There were two 2710-s recording windows every day, whether or not transmissions were scheduled, with data acquisition beginning 10 s before 0000 UTC and 1200 UTC. Each transceiver, therefore, recorded both its own transmissions, those from the other source, and ambient sound. The sample rate was 976.5625 Hz. The actual source levels were determined from the signals recorded on the DVLAs located below the sources (Appendix). The rms source levels were 192 dB re 1 μPa at 1 m for SIO1 and 194 dB re 1 μPa at 1 m for NERSC1.

Two-oscillator systems were used to maintain precise time (Munk *et al.*, 1995). When combined with pre- and post-cruise clock checks, the clock error reaches a maximum value of 1–2 ms in the middle of the experiment and varies smoothly over the year.

The travel times were corrected for mooring displacements measured using long-baseline acoustic navigation systems. Four acoustic transponders (Teledyne Benthos, North Falmouth, MA) on the seafloor around each transceiver mooring were used to determine the source and Hydrophone Module positions. The transponder positions at the SIO moorings were surveyed using interrogations from an acoustic transducer rigidly attached to the *USCGC Healy*. The ship's position was determined using the Global Navigation Satellite System (GNSS), and the ship's heading was used to correct for the offset between the location of the GNSS antenna and the acoustic transducer. The transponder positions at the NERSC moorings were surveyed using interrogations from an acoustic transducer suspended from the *KV Svalbard*. A GNSS antenna was located directly above the acoustic transducer to determine its position. The estimated absolute accuracy of the transponder positions (WGS84) was 3 m rms. The controller in each source and the controller(s) in each DVLA independently interrogated the bottom transponders once per hour. The replies were recorded by both the controllers and the Hydrophone Modules. In addition to a bias in the instrument positions at each mooring due to the uncertainty in the transponder positions, there is an uncertainty of about 1 m that is uncorrelated from measurement to measurement. The mooring displacements used to correct the travel times were computed relative to reference locations that were close to, but not necessarily identical to, the mooring anchor locations (Table I). StableMoor® subsurface mooring buoys (DeepWater Buoyancy, Biddeford, Maine) with a nominal depth of 45 m were used to support the transceiver moorings, and horizontal and vertical (Fig. 2) displacements were typically relatively small.

2. DVLA receiver moorings

The DVLA arrays on SIO2 and SIO3 were identical to the array on SIO1, except that the absence of acoustic

TABLE II. Ranges (km) between the source (SIO1 and NERSC1) and receiver mooring motion reference locations (WGS84).

	SIO3	SIO2	SIO1	NERSC1	NERSC3	NERSC2
SIO1	877.028	350.928	0	1688.829	1749.833	1851.808
NERSC1	2565.699	2039.614	1688.829	0	70.953	176.205

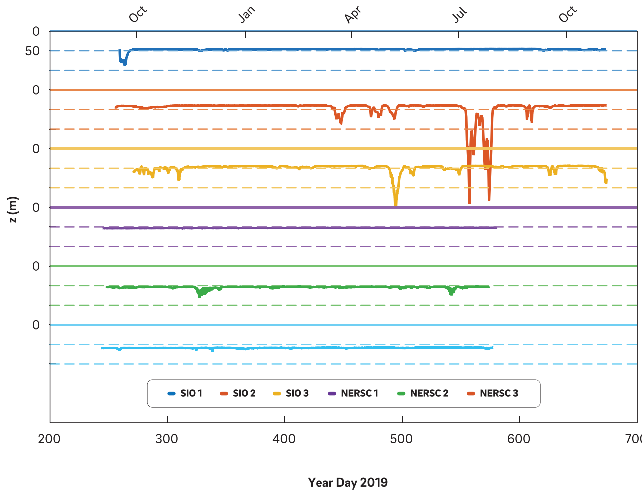

FIG. 2. Depths of Sea-Bird MicroCATs (SBE 37-SMP) (Sea-Bird Scientific, Bellevue, WA) located 5.1 m below the subsurface floats on the moorings vs year day (year day 1 is defined as 1 January 2019). The year days continue into 2020. The plots are successively offset by 150 m, with SIO1 at the top, followed in order by SIO2, SIO3, NERSC1, NERSC2, and NERSC3.

sources allowed the top Hydrophone Module to be placed closer to the surface, i.e., 1 m below the Sea-Bird MicroCAT that was located 5.1 m below the subsurface float. The DVLA arrays on NERSC2 and NERSC3 were identical to the array on NERSC1, except that the top Hydrophone Module was again placed 1 m below the Sea-Bird MicroCAT located below the subsurface float. Long-baseline acoustic navigation systems identical to those used to track the motions of SIO1 and NERSC1 (except that NERSC2 and NERSC3 had three instead of four acoustic transponders) determined the controller and Hydrophone Module positions. The horizontal and vertical (Fig. 2) motions of the DVLA receiver moorings were somewhat larger than those of SIO1 and NERSC1 because spherical subsurface mooring buoys with a nominal depth of 45 m were used to support the DVLA receiver moorings.

B. Signals and signal processing

Pulse compression techniques were used to improve the signal-to-noise ratios of the receptions without degrading the signal resolution. The GTI C-BASS M72–1000 sources transmitted phase-coded, periodic binary *m*-sequences with a center frequency of 35.0 Hz (Table III) (Munk *et al.*, 1995). The transmissions lasted 874.286 s to provide an adequate signal-to-noise (SNR) ratio, which, for a matched filter, depends on the total energy in the signal. Each digit in the *m*-sequence contained eight cycles of the 35 Hz carrier, giving a temporal resolution after pulse compression of 8/35 s. The signals differed only in the sequence laws used. The approximate full bandwidth of the signals, given by $1/T$ where T is the digit length, is 4 Hz.

The phase modulation angle was defined to be $\tan^2\theta_0 = L$, giving a smooth sinc^2 envelope to the power spectrum (Munk *et al.*, 1995). The autocorrelation function

TABLE III. Parameters of the phase-coded, periodic binary *m*-sequence signals transmitted by the GTI sources on the SIO1 and NERSC1 moorings.

Carrier frequency (Hz)	35.0
Cycles/digit	8
Digit length (s)	8/35
Sequence length L (digits)	255
Sequence period (s)	58.2857
Sequence law	SIO1: 537_8 NERSC1: 717_8
Phase modulation angle θ_0	86.416678°
Sequence repetitions	15
Transmission duration (s)	874.286

of the modulating sequence is then identically zero at nonzero lags, i.e., there is no self-clutter in the time domain following pulse compression.

The received signals were complex demodulated to baseband using the carrier frequency of 35.0 Hz. The phase modulation was then removed using a phase-only filter, i.e., factor inverse filtering (FIF) (Birdsall and Metzger, 1986; Munk *et al.*, 1995). Twelve of the 15 sequences were coherently summed, avoiding end effects at the beginning and end of the periodic transmissions. The nominal SNR gain from the pulse compression is then $10\ \log_{10}\ (255 \times 12) = 34.9$ dB. Figures 3, 4, and 5 show measured and predicted receptions at SIO3 for transmissions from SIO1 (SIO1-SIO3), at SIO1 for transmissions from NERSC1 (NERSC1-SIO1), and at SIO3 for transmissions from NERSC1 (NERSC1-SIO3), respectively.

The predicted receptions were generated for sound-speed sections computed from the WOA 2023 objectively analyzed mean temperature and salinity fields on a 1/4° grid for the decade 2015–2022 (Locarnini *et al.*, 2024; Reagan *et al.*, 2024a; Reagan *et al.*, 2024b). An adiabatic,

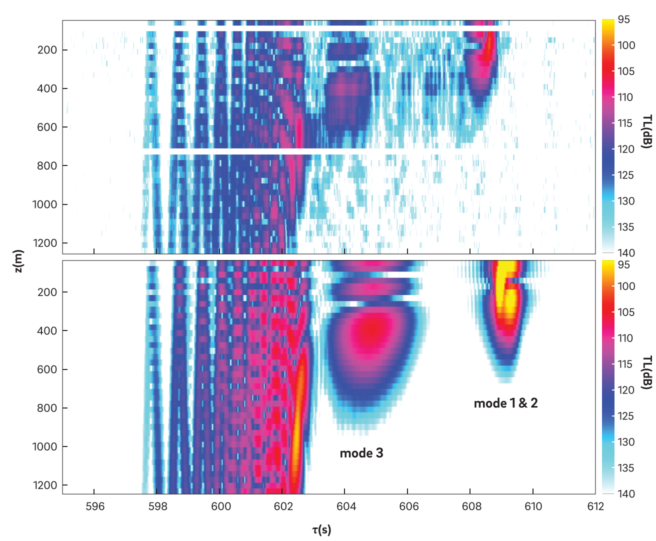

FIG. 3. Measured (top) and predicted (bottom) receptions at SIO3 for transmissions from SIO1. TL is shown as a function of travel time τ and depth z. The measured reception is for the SIO1 transmission on 20 August 2020. The predicted reception was generated for the sound-speed section computed from the WOA 2023 1/4° grid for the decade 2015–2022.

https://doi.org/10.1121/10.0042233

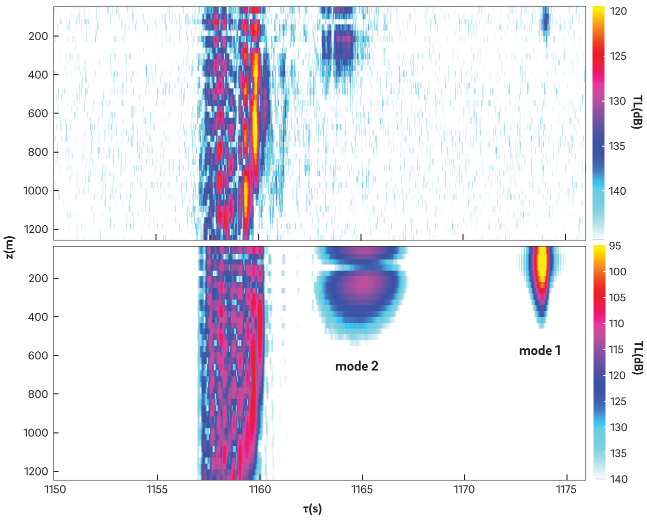

FIG. 4. Same as Fig. 3 except for the measured reception at SIO1 for the transmission from NERSC1 on 24 September 2019.

range-dependent normal mode propagation code was used to make the predictions. For simplicity, a pressure-release (perfectly reflecting) sea surface was assumed in the simulations, ignoring the effects of the sea ice. The predicted transmission loss (TL) is not expected to be accurate without including scattering from the ice cover, but the basic structure of the predicted receptions as a function of depth and travel time is expected to be accurate. There is a large literature on the effects of scattering from a rough sea-ice cover, and comparisons of measured and predicted TL are left for future work. The Lomonosov and Alpha Ridges rise to depths of approximately 1200 and 1800 m, respectively, on the acoustic path from NERSC1 to SIO3. The Lomonosov Ridge appears to be slightly deeper (1400 m) on the path from NERSC1 to SIO1, although the bathymetry is not well known. In any event, these ridges block acoustic modes above approximately mode number 30, and these high-order

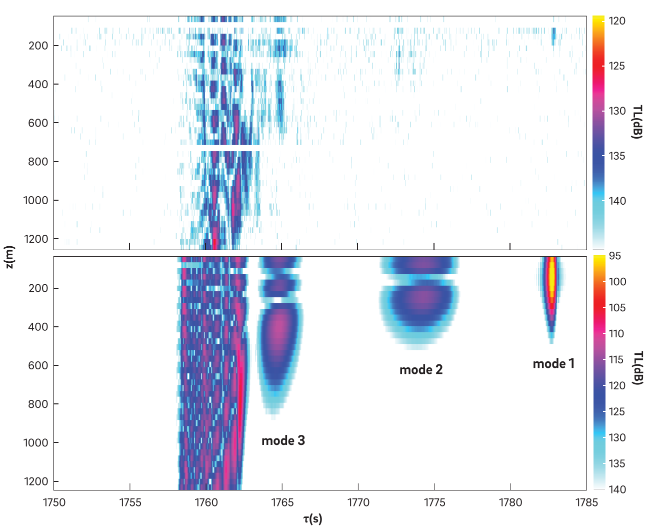

FIG. 5. Same as Fig. 3 except for the measured reception at SIO3 for the transmission from NERSC1 on 8 November 2019.

modes were therefore omitted from the predicted receptions for these paths.

The observed and simulated receptions show common features. Late-arriving, low-order normal mode arrivals are evident at all three ranges (modes 1, 2, and 3). In the western Arctic, mode 3 is highly dispersed (SIO1-SIO3) (Fig. 3). In the eastern Arctic, however, mode 2 experiences the most dispersion (NERSC1-SIO1) (Fig. 4). The predicted arrival pattern for the trans-Arctic transmissions (NERSC1-SIO3) (Fig. 5) shows that both modes 2 and 3 are expected to be significantly dispersed, but the SNR is sufficiently low that this is difficult to see in the measured receptions. Finally, early-arriving, high-angle time fronts are evident in the measured and predicted arrival patterns for the acoustic path entirely in the western Arctic (SIO1-SIO3). This acoustic path is in the Canada Basin and does not have significant bathymetric obstructions. High-angle time fronts (or, equivalently, high-order modes) are absent from the receptions for the acoustic paths from NERSC1 to SIO1 and NERSC1 to SIO3, however. On these paths, blocking due to the Lomonosov and Alpha Ridges eliminates the high-angle time fronts that would otherwise be present in the observed and simulated receptions. In all three cases, the measured TL exceeds the predicted TL because the loss due to interactions with the ice-covered surface was not accounted for in the predictions.

III. OCEANOGRAPHIC ENVIRONMENT

The ocean stratification and sea ice in the eastern and western Arctic Ocean differ, with significant implications for acoustic propagation (e.g., Worcester and Ballard, 2020). Environmental data obtained during CAATEX reflect these differences.

A. Ocean stratification

Figure 6 shows the full-depth conductivity-temperature-depth (CTD) casts that were made near SIO1, SIO3, and NERSC3 during the mooring deployment cruises. These profiles illustrate the typical differences in ocean stratification between the eastern and western Arctic Ocean. In the eastern Arctic, there is a 100–200 m thick layer of cold Polar Water (PW) immediately under the ice. Below the PW, much warmer waters entering the Arctic Ocean through Fram Strait and the Barents Sea Opening result in a temperature maximum associated with the Atlantic Water (AW). In the Beaufort Sea in the western Arctic, a layer of relatively warm, high sound-speed Pacific Summer Water (PSW) at about 80 m depth lies above colder, more saline, and lower sound-speed Pacific Winter Water (PWW) located between roughly 100 and 200 m depth. Below the PWW is the AW, with a second temperature maximum near 400 m depth (McLaughlin *et al.*, 2011). (The AW is much cooler and deeper in the western Arctic than it is close to the source regions in the eastern Arctic.) The result is a sound-speed minimum, the Beaufort Duct, at a depth of roughly 150 m (Freitag *et al.*, 2015). The CTD cast at SIO3 (western

https://doi.org/10.1121/10.0042233

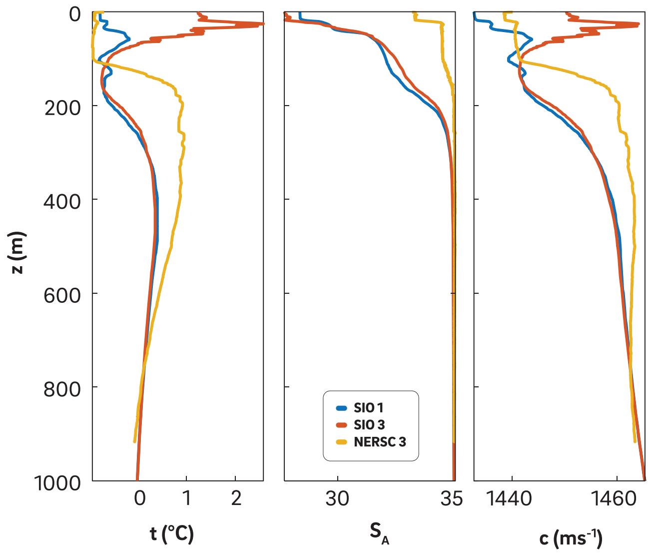

FIG. 6. *In situ* temperature t (ITS-90), Absolute Salinity S_A, and sound-speed c in the upper 1000 m from CTD casts made during the mooring deployment cruises at SIO1, SIO3, and NERSC3. Absolute Salinity and sound speed were computed using the International Thermodynamic Equation of Seawater – 2010 (TEOS-10) (IOC, SCOR, and IAPSO, 2010).

Arctic) has a strong, subsurface sound-speed duct with a minimum extending from about 100 to 160 m (Fig. 6). Further north at SIO1, closer to the North Pole, the temperature maximum associated with the PSW is much weaker, and the Beaufort Duct has almost disappeared.

The differing stratification in the eastern and western Arctic Ocean is also evident in the extensive temperature and salinity measurements made at each mooring. Sea-Bird instruments measuring temperature and, in some cases, salinity extended from a depth of about 50 m (Sea-Bird SBE 37-SMP located 5.1 m below the subsurface floats) to a maximum depth of approximately 1000 m. In addition, the Hydrophone Modules on the moorings made temperature measurements (±0.005 °C) at 20-min intervals (Fig. 7). In the western Arctic, considerable temperature variability is present at the depth of the PSW at both the transceiver mooring SIO1 and the receiver mooring SIO3, but the PWW temperature is much more stable (Kucukosmanoglu *et al.*, 2023) (Fig. 7). The temperatures at the shallow Hydrophone Modules at the transceiver mooring NERSC1, which are in the PW, are also quite variable (Fig. 7). (The CTD cast at receiver mooring NERSC3 rather than at NERSC1 is shown in Fig. 6 because a CTD cast was not made near NERSC1 due to difficult ice conditions.)

B. Sea ice

The subsurface floats supporting the moorings had 420-kHz ASL Environmental Sciences IPS-5 (ASL, Saanichton, Canada) ice profiling sonars to determine ice draft (using the procedures described in Krishfield *et al.*, 2014) and upward-looking RDI Workhorse Sentinel 600-kHz ADCPs (Teledyne RD Instruments, Poway, CA) to measure upper ocean currents and sea ice velocities. The precision pressure

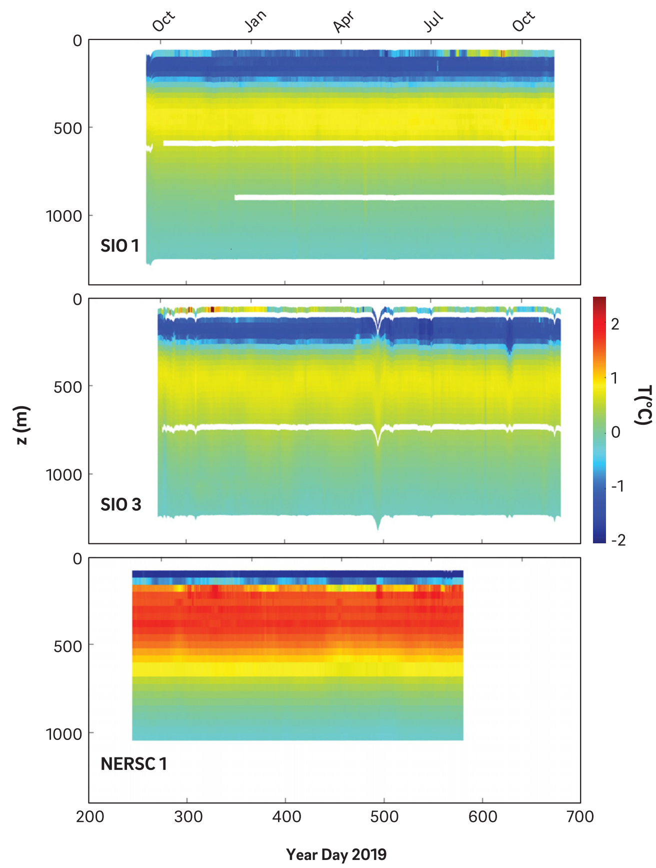

FIG. 7. *In situ* temperature measured by the Hydrophone Modules at moorings SIO1 (top), SIO3 (middle), and NERSC1 (bottom) vs year day 2019.

sensors in the IPS-5 profiling sonars were damaged in a previous deployment, and the pressure sensors in the Sea-Bird MicroCATs located 5.1 m below the subsurface floats were used instead to compute ice drafts, slightly degrading the accuracy (Worcester *et al.*, 2024).

Somewhat surprisingly, the daily median ice drafts reached similar maximum values that were close to 2 m at all moorings despite the quite different locations (Fig. 8).

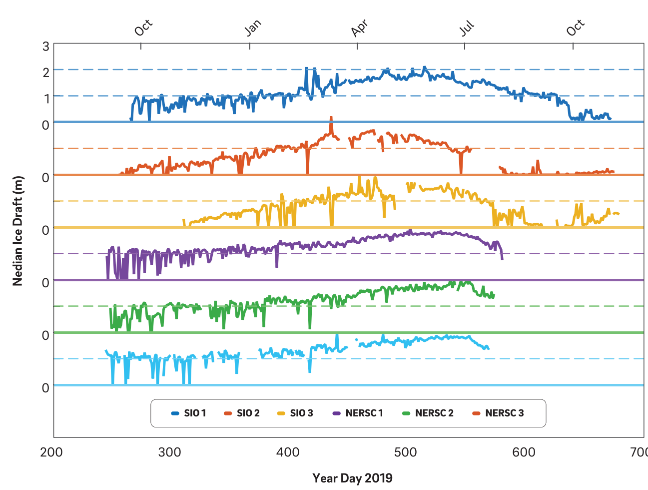

FIG. 8. Daily median ice drafts from the IPS-5 ice-profiling sonars. The plots are successively offset by 2 m, with SIO1 at the top, followed in order by SIO2, SIO3, NERSC1, NERSC2, and NERSC3.

NERSC1, NERSC2, and NERSC3 were located relatively close together and behaved similarly, with considerable variability in the late summer and early fall of 2019 and maximum ice drafts in June 2020. SIO1, SIO2, and SIO3 spanned a much wider range of latitudes, and the ice drafts behaved somewhat differently at each site. SIO1, the northernmost mooring, was covered by ice almost the entire time, except perhaps for a short period of thin ice in October 2020. SIO2 and SIO3 showed longer periods of open water in late summer and early fall of 2019 and/or 2020.

IV. MODAL TRAVEL-TIME SERIES

The procedure used to generate time series of modal group delays (travel times) is described in detail in Akins *et al*. (2025) and will only be briefly summarized here. First, the low-order normal mode arrivals were extracted from the receptions on the vertical receiving arrays using a combination of windowing in time and spatial filtering. Because the group velocities of some of the modes varied significantly across the signal bandwidth, resulting in dispersed modal arrivals with poorly defined arrival times (Figs. 3, 4, and 5), the next step was to jointly estimate the travel time at the center frequency (35 Hz) and a parameter characterizing the dispersion. Outliers with low signal-to-noise ratio (SNR) were then removed to give time series of the estimated travel times vs year day.

A. Normal Mode Filtering

Conventional sampled mode shape mode filters were applied to isolate the normal modes in the receptions on the vertical receiving arrays (e.g., Buck *et al*., 1998). Prior to spatial filtering, the received data were windowed around the nominal arrival times using a Tukey window with $\alpha = 0.5$ (Harris, 1978). A 4-s window (±2 s) was used for the shorter SIO1-SIO3 receptions, and a 6-s window (±3 s) was used for the NERSC1-SIO1 and NERSC1-SIO3 receptions. This minimizes crosstalk from high-order modes that are not well resolved by the array (Wage *et al*., 2003).

The mode shapes used in the sample mode shape mode filters were computed for each reception using Hydrophone Module and Sea-Bird MicroCAT data to allow for variations in mode shapes over the year. The sound-speed profiles needed to compute the mode shapes were obtained by projecting temperature data from the Hydrophone Modules (Fig. 7) and temperature and salinity data from the Sea-Bird MicroCATs on each mooring on a basis of empirical orthogonal functions (EOFs), which were computed using a combination of CAATEX and historical data.

Background or reference temperature and salinity profiles were first constructed. In the depth range 0–700 m, historical Ice Tethered Profiler (ITP) data (Krishfield *et al*., 2008) were used for this purpose. In the depth range 700–1200 m, the CAATEX thermistor data (Fig. 7) together with a temperature-salinity relationship from the CAATEX CTD data were used. Finally, in the depth range 1200–3000 m, a combination of the CAATEX CTD data and historical CTD data was used. The historical CTD data were obtained in 2015 by the *USCGC Healy* (cruise 33HQ20150809).

EOFs were then computed. In the depth range 0–700 m, the differences between the ITP data and the reference temperature and salinity profiles were used to compute EOFs. Below 700 m, the differences between the CAATEX and historical CTD data and the reference profiles were used to compute EOFs. Next, the differences between the reference profiles and the Hydrophone Module temperatures and the Sea-Bird MicroCAT temperatures and salinities were fit to the EOF basis functions every 20 min at the times of the Hydrophone Module temperature measurements. Finally, sound-speed profiles were computed for each mooring using the International Thermodynamic Equation of Seawater–2010 (TEOS-10) (IOC, SCOR, and IAPSO, 2010). This procedure gives full-water-column sound-speed profiles, making computation of normal mode shapes straightforward. Normal mode shapes computed for the sound-speed profile closest in time to each reception (but neglecting any effects due to the sea ice) were used to construct the sample mode shape filters.

Although mode shapes were computed for each reception to implement the spatial filtering, the mode shapes did not vary significantly over the year, and the results were not sensitive to doing so (not shown). For reference, Fig. 9 shows the mode shapes at 35 Hz computed using the deployment cruise CTD profiles shown in Fig. 6. The sampled mode shape correlation matrices for the modes in Fig. 9 show that modes 1 through 6 are well resolved by the vertical receiving arrays on moorings SIO1 and SIO3 (Fig. 10).

B. Joint group delay/dispersion estimation

As is evident in Figs. 3, 4, and 5, the CAATEX signal bandwidth is sufficiently large that geometric dispersion substantially broadens the received waveform for mode 3 in the western Arctic and mode 2 in the eastern Arctic. Modes

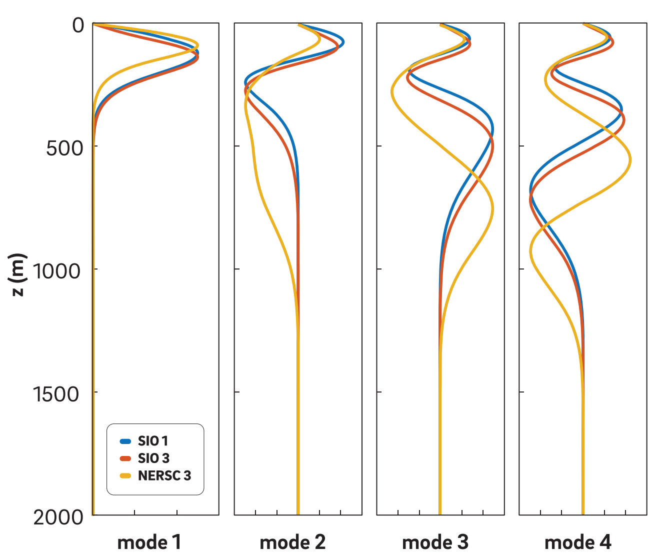

FIG. 9. Normal mode functions 1–4 at 35 Hz at SIO1, SIO3, and NERSC3 computed using deployment cruise CTD profiles close to each mooring.

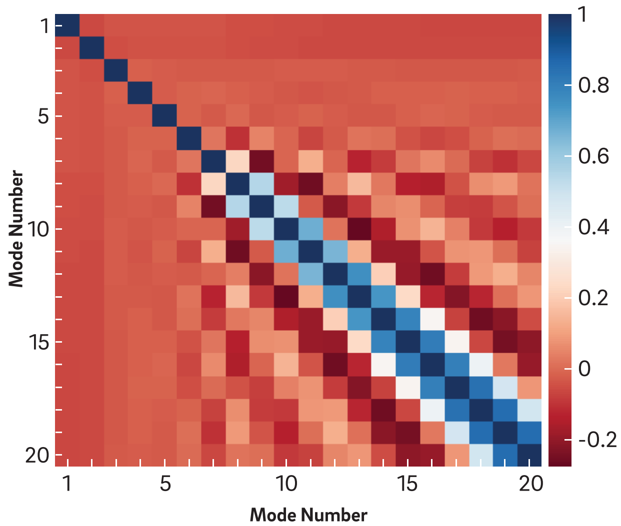

FIG. 10. Sampled mode shape correlation matrix at 35 Hz at SIO1 computed using normal mode shapes for the deployment cruise CTD profile at SIO1 shown in Fig. 6. The correlation matrix at SIO3 is similar, because the receiving arrays at SIO1 and SIO3 are identical and the sound-speed profiles are relatively similar.

2 and 3 both experience significant dispersion in the trans-Arctic transmissions. Dispersion curves showing group delay vs frequency in the vicinity of the CAATEX center frequency of 35 Hz for SIO1-SIO3, NERSC1-SIO1, and NERSC1-SIO3 are shown in Fig. 11. These dispersion curves were generated using sound-speed sections derived from the WOA 2023 1/4° grid for the decade 2015–2022 assuming adiabatic propagation and neglecting any effects due to sea ice, as was the case for the predicted arrival patterns in Figs. 3, 4, and 5. The expected dispersion for mode 3 in the western Arctic and mode 2 in the eastern Arctic, approximately given by the change in group delay over the full bandwidth of the signal (~ 4 Hz), i.e., between 33 and 37 Hz, is much greater than the digit length (8/35 s) (Table III). The implication is that the received signal for the dispersed modes is no longer a simple replica of the transmitted signal, and estimation of the group delay at the center frequency (i.e., travel time) by picking the peak of the distorted arrival is no longer justified.

In response, Akins *et al.* (2025) developed a procedure for joint delay and dispersion estimation that was applied to each mode after spatial filtering. The procedure takes advantage of the low internal-wave energy level in the Arctic Ocean, so that internal-wave-induced scattering of the acoustic signal is small (e.g., Colosi, 2016). The group delay and dispersion of each mode can then be treated as deterministic unknown parameters to be estimated, as is done in the common signal processing problem of joint delay and Doppler estimation. Hermand and Roderick (1993) previously developed matched filters for dispersed signals using a model-based approach. Akins *et al.* (2025), however, used a parameter-estimation approach that does not rely on model predictions of the modal dispersion.

Although the CAATEX bandwidth is large enough that dispersion is important, the bandwidth is small enough that

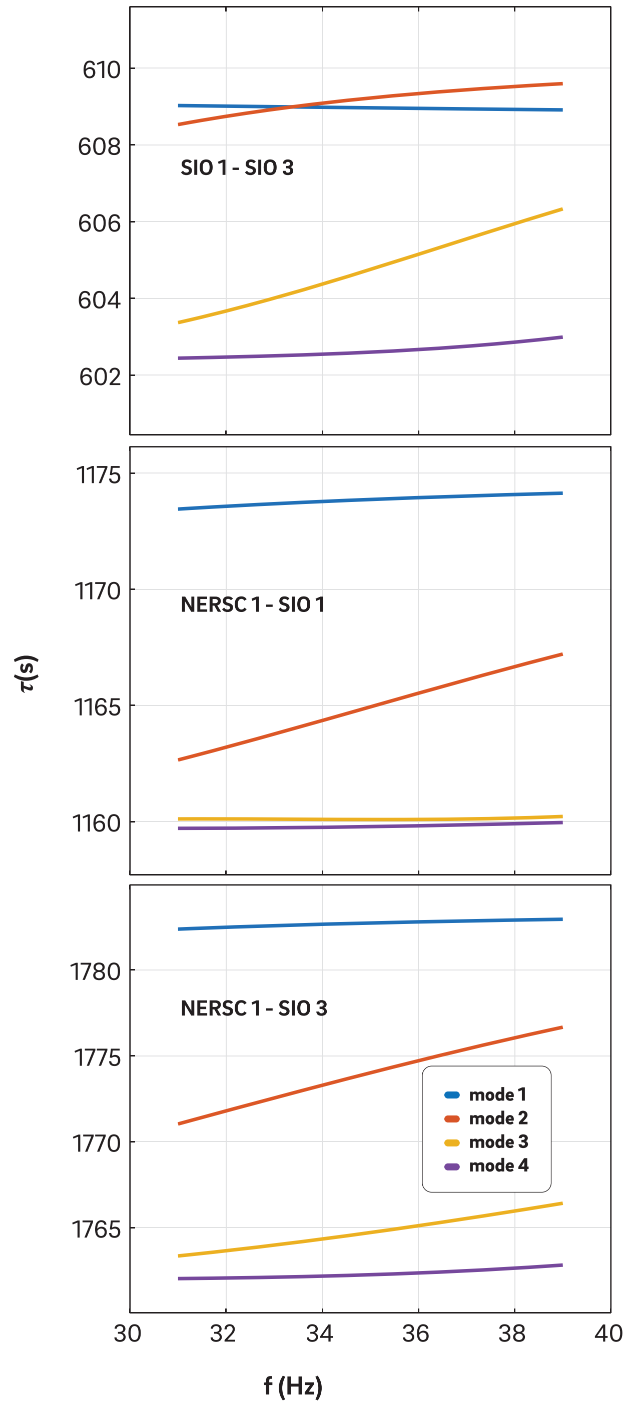

FIG. 11. Group delay vs frequency for modes 1–4 for SIO1-SIO3 (top), NERSC1-SIO1 (middle), and NERSC1-SIO3 (bottom). The dispersion curves were generated for the sound-speed section derived from the WOA 2023 1/4° grid for the decade 2015–2022.

the group delay τ is a nearly linear function of frequency (Fig. 11), so that the dispersion can be characterized by a single dispersiveness parameter β. The modal group delay at the center frequency can then be estimated by maximizing the output of a matched filter over a set of replica waveforms with differing β. When processing the CAATEX receptions, the additional assumption was made that β was constant over the experiment. The maximum likelihood

https://doi.org/10.1121/10.0042233

estimate $\widehat{\beta}$ applicable to the full experiment was obtained by maximizing the sum of the squared matched filter peak outputs over all transmissions. As shown in Akins *et al.* (2025), this procedure resulted in dramatic improvements in the group delay estimates $\widehat{\tau}$ at the center frequency for the highly dispersed modes, as well as in a nearly 6 dB increase in matched filter output power.

C. Modal group delay series

The group delay estimates $\widehat{\tau}$ at 35 Hz resulting from the procedure described previously are shown vs year day in Figs. 12, 13, and 14 for modes 1 through 4 for transmissions from SIO1 to SIO3, from NERSC1 to SIO1, and from NERSC1 to SIO3, respectively. As discussed in Sec. II, the group delays have been corrected for clock drifts and mooring displacements. Outliers with low SNR have been removed from the time series, but some apparent outliers remain. The gaps in the modal time series for SIO1-SIO3 between year days 500 and 600, which are especially clear for modes 1 and 2, are due to a malfunction of the source on SIO1.

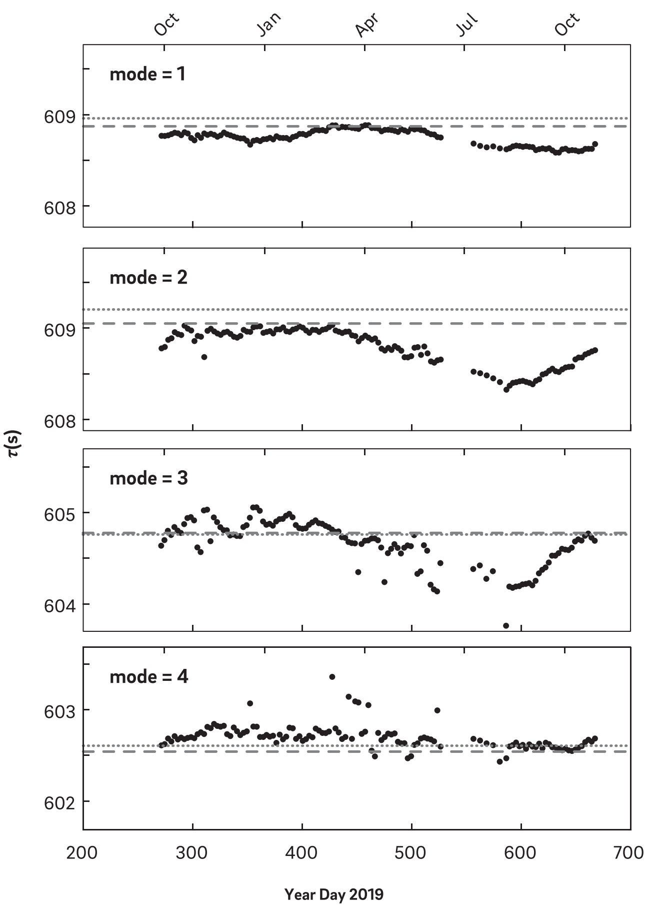

FIG. 12. Modal group delays (travel times) at 35 Hz for modes 1 through 4 vs year day 2019 for transmissions from SIO1 to SIO3. The predicted travel times calculated using the WOA 2023 temperature and salinity fields for the decade 2015–2022 on 1/4° (dotted) and 1° (dashed) grids are also shown. The vertical axis spans 2 s full scale in all cases. The uncertainty of the measured travel-times calculated using the standard Cramer-Rao Lower Bound (CLRB) (Helstrom, 1968) for an SNR of 30 dB and rms bandwidth of 1.5 Hz is 0.002 s. The total travel-time uncertainty also includes contributions from uncertainties in the mooring positions (~5 m) and the clocks (~0.002 s). Assuming independent errors, the total travel-time uncertainty is ~0.005 s.

The SIO1-SIO3 acoustic path has the shortest range (877.028 km, Table II) of those shown here. The mode 1 travel time varies by relatively little over the year, but the mode 2 and 3 travel times vary by close to 1 s. The mode shapes in Fig. 9 suggest that these modes are sensitive to perturbations in the PSW and the AW, but a proper interpretation using inverse methods is left for a future paper. The mode 4 travel time is relatively stable, at least in part because this mode extends to greater depth, where the sound speed is expected to be nearly constant, than the lower-order modes.

Unlike the nearly complete travel-time series obtained for SIO1-SIO3, the mode 1 arrivals for NERSC1-SIO1 disappear at the beginning of January 2020 and only reappear in two receptions shortly before the mooring was recovered. This path is nearly twice as long (1688.829 km, Table II) as the SIO1-SIO3 path. Nonetheless, the time series for modes 2, 3, and 4 are still relatively complete. Mode 1 interacts more strongly with the ice than the higher-order modes, and the ice drafts at SIO1 (Fig. 8), which are the only

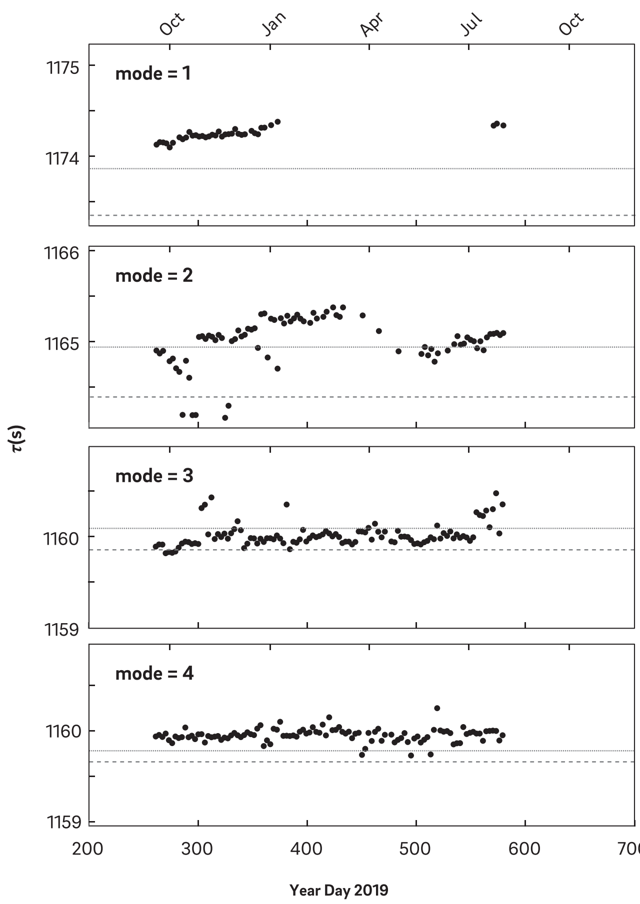

FIG. 13. Same as Fig. 12 except for transmissions from NERSC1 to SIO1. The uncertainty of the measured travel-time calculated using the standard CRLB for an SNR of 10 dB and rms bandwidth of 1.5 Hz is 0.017 s. Uncertainties in the mooring positions and clock timing are negligible in this case.

https://doi.org/10.1121/10.0042233

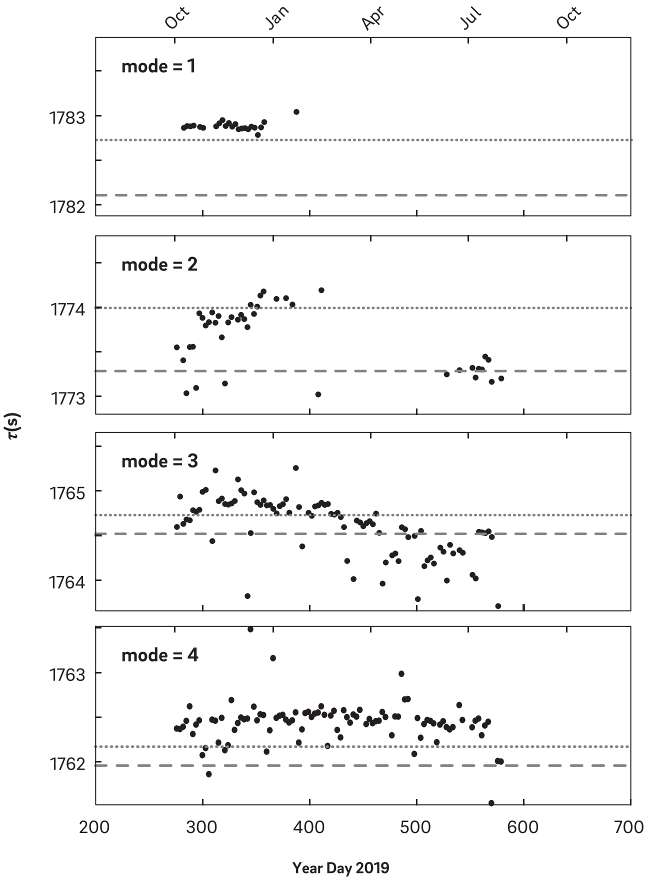

FIG. 14. Same as Fig. 12 except for transmissions from NERSC1 to SIO3. The uncertainty of the measured travel-time calculated using the standard CRLB, with an SNR of 5 dB and rms bandwidth of 1.5 Hz is 0.030 s. Uncertainties in the mooring positions and clock timing are negligible in this case.

measurements of ice draft in the central Arctic during CAATEX, do not return to their values at the beginning of January 2020 until about the time that the NERSC1 mooring was recovered. Enhanced scattering associated with the greater ice drafts may therefore account for the disappearance of the mode 1 arrivals. The travel times of modes 1, 3, and 4 are relatively stable, but mode 2 travel times vary by roughly 0.5 s.

Finally, the mode 1 and 2 arrivals for NERSC1-SIO3 behave somewhat similarly to the mode 1 arrivals for NERSC1-SIO1, disappearing at the beginning of January 2020. Mode 2 reappears in late summer, however. This path has the longest range (2565.699 km, Table II) and, presumably, the greatest loss due to scattering from the ice. The travel time of mode 3 varies by roughly 1 s and that of mode 2 by roughly 0.5 s, but there is considerable scatter in the travel-time measurements at this long range.

Note that for all three ranges, there are no outliers in the time series for mode 1. The outliers appear to occur preferentially in the mode 2 and mode 3 time series, which could indicate that those modes are not propagating adiabatically. If this is the case, it is unlikely that mode coupling is due to bathymetric interactions. There is no significant bathymetry on the path from SIO1 to SIO3. Although the Lomonosov and Alpha Ridges are on the paths from NERSC1 to SIO1 and NERSC1 to SIO3, the ridges are too deep to cause mode coupling for the low-order modes at 35 Hz. As noted in Sec. II B, the Lomonosov Ridge rises to a minimum depth of about 1200 m on these paths, but the low-order modes do not extend to that depth (Fig. 9). If mode coupling is occurring, it is therefore likely due to sound-speed perturbations in the upper ocean at the depths to which modes 2 through 4 are sensitive. Given the low internal-wave energy levels in the Arctic Ocean, these perturbations are likely due to mesoscale structure (e.g., Kucukosmanoglu *et al.*, 2023).

For comparison, the predicted travel times calculated using the WOA 2023 temperature and salinity fields for the decade 2015–2022 on 1/4° and 1° grids are also shown in Figs. 12, 13, and 14. The measured modal group delays provide a stringent test of the accuracy of the WOA 2023 fields along the acoustic paths. Predicted modal group delays for SIO1-SIO3 using the two grids give similar results and are reasonably consistent with the measured group delays for all four modes, given the observed variability in the group delays over the year. For NERSC1-SIO1 and NERSC1-SIO3, the predicted delays for modes 3 and 4 using the two grids also give similar results and are reasonably consistent with the measured group delays. The modal group delays predicted using the 1/4° grid are in much better agreement with the measured group delays for modes 1 and 2 than those predicted using the 1° grid, however.

The radius of influence used to construct the fields in WOA 2023 is much larger for the 1° grid (446 km) than for the 1/4° grid (214 km) (Locarnini *et al.*, 2024; Reagan *et al.*, 2024a; Reagan *et al.*, 2024b). Given the sparsity of data in the Arctic Ocean (Figs. 15 and 16), there is a trade-off between the 1° grid, which uses more data to construct each profile, and the 1/4° grid, which uses less data to construct each profile but uses data closer to each grid point. One possible cause of the poorer performance of the 1° grid for transmissions from NERSC1 is that the radius of influence is sufficiently large that data from north of Svalbard and in the Fram Strait, where the warm West Spitzbergen Current enters the Arctic Ocean, are biasing the 1° grid fields.

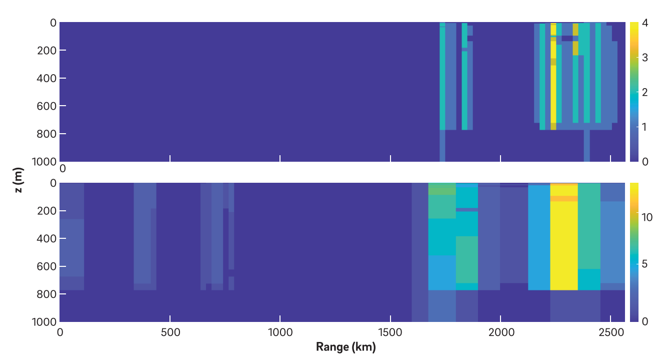

FIG. 15. Number of grid squares on the acoustic path from NERSC1 to SIO3 containing temperature data for the WOA 2023 1/4° (top) and 1° (bottom) grids. NERSC1 is on the left at 0 km range, and SIO3 is on the right. Note the different color bars.

https://doi.org/10.1121/10.0042233

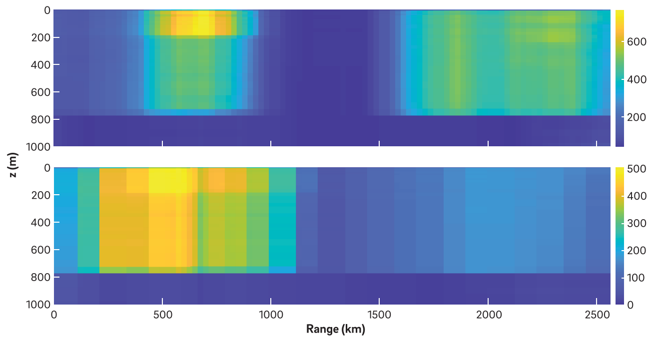

FIG. 16. Same as Fig. 15, except for the number of grid squares within the radius of influence of the acoustic path from NERSC1 to SIO3 containing temperature data.

V. TRAVEL TIMES: TAP AND CAATEX

The NERSC3 and SIO3 positions (Table I) were chosen to be close to the nominal source (TURPAN) and receiver (SIMI) ice camp locations during the 1994 TAP experiment. The ice camps were drifting, of course, but at the time of TAP transmission #23, which occurred at 1300 UTC on 20 April 1994 (year day 110), the source was at 83.352°N, 25.070° E, and the receiver was at 73.008°N, 149.572°W (Mikhalevsky *et al.*, 1999). The source depth was 60 m. The NERSC1 source was located to the north of NERSC3, but the transmissions from NERSC1 to SIO3 followed essentially the same acoustic path as the TAP transmissions. The range from NERSC1 to SIO3, however, was slightly shorter than the range from TURPAN to SIMI (see Fig. 1). Modal group delays at the differing frequencies employed in CAATEX (35 Hz) and TAP (19.6 Hz) cannot be directly compared because the mode shapes differ significantly (Figs. 9 and 17). The modes at 19.6 Hz extend deeper into the water column than those at 35 Hz. The sensitivities of the group velocities to the sound-speed structure are therefore different. Comparisons with travel times predicted for TAP using sound-speed fields derived from WOA 2023 are therefore reported here. Inversions of the CAATEX travel times to obtain range-averaged temperature fields between the moorings are left for a subsequent paper.

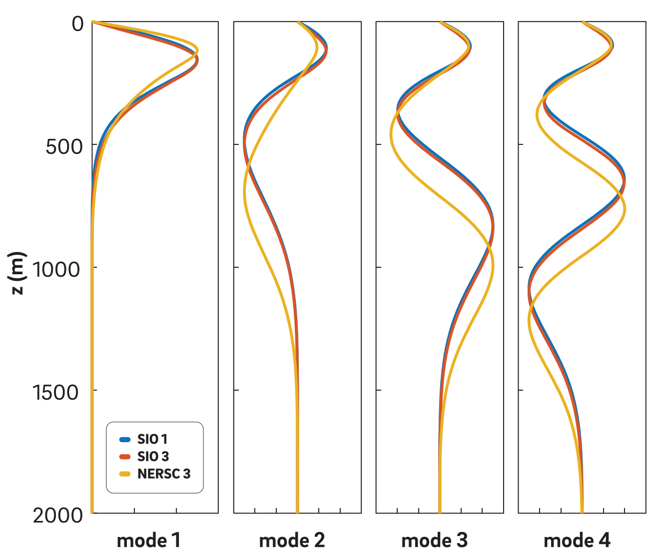

FIG. 17. Normal mode functions 1–4 at 19.6 Hz (TAP) at SIO1, SIO3, and NERSC3 computed using CAATEX deployment cruise CTD profiles close to each mooring.

In Sec. IV, the CAATEX travel times for NERSC1-SIO3 were found to be in relatively good agreement with predictions made using the WOA 2023 temperature and salinity fields on a 1/4° grid for the decade 2015–2022 (Fig. 14). Travel time predictions made using the WOA 2023 1° grid were not as good, particularly for modes 1 and 2. Here, the travel times for modes 1–4 at 19.6 Hz reported for TAP (Mikhalevsky *et al.*, 1999) are compared with travel times computed assuming adiabatic propagation and using both the 1/4° and 1° grids from WOA 2023 (Fig. 18). The TAP travel times are the average of twelve transmissions after correction to a reference range of 2637.500 km, which was the range between TURPAN and SIMI at the time of transmission #23.

Mikhalevsky *et al.* (1999) estimated the uncertainty of the TAP mode travel times to be ±1.0 s to ±1.3 s, depending on the mode. The source at TURPAN was manually synchronized to GPS, giving an estimated uncertainty of ±1 s. The additional uncertainty reflects the variability in the travel times of the 12 transmissions. Mikhalevsky *et al.* (1999) reported mode 2 travel times that were significantly shorter than those computed from the Arctic Ocean climatology available at the time, implying warming of the AW compared to climatology. Figure 18 shows that the TAP mode-2 travel time is consistent with the travel times across all decades as predicted using WOA 2023, however, given the large estimated uncertainty in the TAP travel time. It is therefore impossible to infer a trend from the TAP mode-2 travel time and the WOA 2023 data. WOA 2023 is not the truth, of course, given the sparsity of the hydrographic data in the Arctic Ocean (Figs. 15 and 16), which only gets worse in earlier decades. Attempts to infer a trend are also difficult because the TAP data were obtained over a few days in April 1994, while the CAATEX data show travel-time variability over the year-long deployment that is a significant fraction of a second for transmissions from NERSC1 to SIO3, particularly for modes 2 and 3 (Fig. 14).

VI. DISCUSSION

The CAATEX experiment has demonstrated that long-range acoustic transmissions provide precise, year-round measurements of travel times under the ice in the Arctic Ocean. The travel times (group delays) of resolved, low-order acoustic normal modes can be measured with accuracies ranging from ~0.005 s for SIO1-SIO3 (877.028 km range) to ~0.030 s for NERSC1-SIO3 (2565.699 km range). (Error bars are not shown for the group delays in Figs. 12, 13, and 14 because the dot sizes are larger than the uncertainties.) The development of a procedure for the joint estimation of the modal group delay at the center frequency (35 Hz) and a parameter characterizing the dispersion of

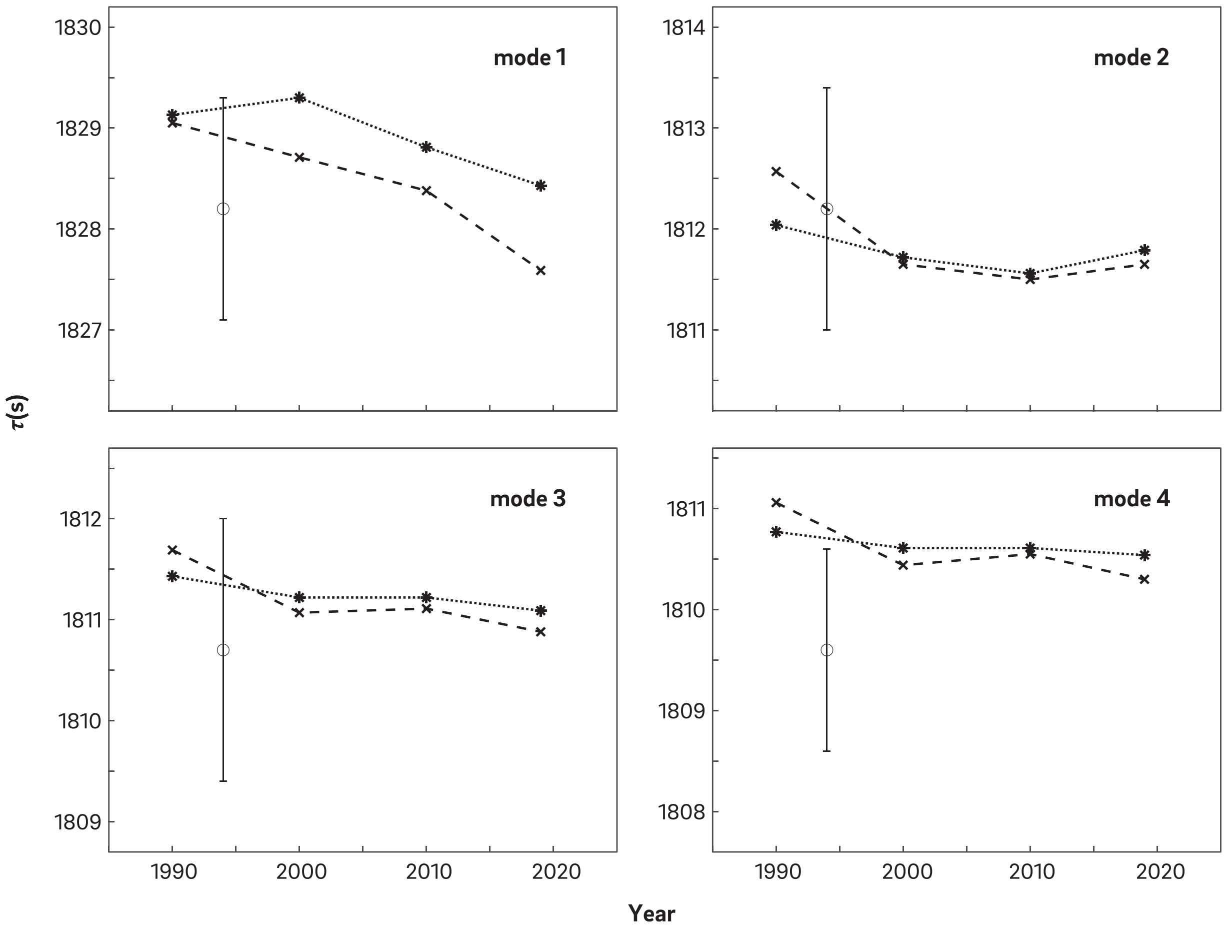

FIG. 18. Travel times (modal group delays) for modes 1–4 for transmissions from TURPAN to SIMI. The measured travel times during the 1994 TAP experiment are shown with the associated uncertainties (open circles with error bars). The travel times derived from the WOA 2023 1/4° (dotted) and 1° (dashed) grids are also shown for the decades 1985–1994, 1995–2004, 2005–2014, and 2015–2022. The vertical axis spans 4 s full scale in all cases.

each mode, as described by Akins *et al.* (2025), was essential to achieving these accuracies, given the substantial temporal dispersion of some of the low-order modes. This procedure also significantly improved the SNR of the dispersed modes.

The SNR for transmissions in the western Arctic from SIO1 to SIO3 were adequate to give essentially complete time series over the year of the group delays of the low-order modes. The SNR for transmissions across the eastern Arctic from NERSC1 to SIO1 (1688.829 km range) and trans-Arctic transmissions from NERSC1 to SIO3 (2565.699 km range) were, however, marginal for the lowest modes at 35 Hz. As a result, travel-time series for mode 1 for NERSC1-SIO1 and modes 1 and 2 for NERSC1-SIO3 are only available for fall 2019, with the SNR dropping to unusable levels around the beginning of January 2020, presumably because these low-order modes suffered more scattering from the ice than higher-order modes as the ice draft and roughness increased in the winter. However, essentially complete time series are available for modes 2, 3, and 4 for NERSC1-SIO1 and modes 3 and 4 for NERSC1-SIO3.

Obtaining highly accurate travel times of resolved modes is the initial step needed to apply inverse methods to obtain the range-averaged sound-speed (temperature) along the acoustic paths over the year. The application of inverse methods using these modal group delays is the next step, but that is left for subsequent papers. These results also have implications for the development of acoustic positioning systems under the ice (e.g., APL-UW, 2008; Mikhalevsky *et al.*, 2015; Howe *et al.*, 2019). The accuracy of any such system depends on the accuracy with which the travel times can be measured.

Finally, when the CAATEX experiment was designed, the intent was to compare range-averaged temperatures derived from the 2019–2020 CAATEX travel times for the NERSC1-SIO3 path (Fig. 14) with those derived from the 1994 TAP data to assess the extent to which the Arctic Ocean had warmed during the intervening decades on the nearly coincident trans-Arctic acoustic paths. As noted previously, the TAP and CAATEX group delays cannot be directly compared because of the differences in the vertical mode shapes and, therefore, the mode weightings at the 19.6 and 35 Hz carrier frequencies, and an indirect method using the group delays computed using WOA 2023 as a convenient standard was therefore attempted here. (This approach automatically corrects for the small difference in the ranges.) The combination of the large uncertainty in the

1994 TAP travel times (approximately ± 1 s), the small changes in the modal travel times at 19.6 Hz predicted using the WOA 2023 1/4° fields of temperature and salinity (Fig. 18), and the modal travel-time variability over the year-long CAATEX deployment (Fig. 14), however, preclude definitive conclusions.

ACKNOWLEDGMENTS

The success of the CAATEX experiment is the result of the efforts of many people, including individuals at the Scripps Institution of Oceanography (L. Green, D. Horwitt, M. Norenberg, and K. Scott), the Naval Postgraduate School (C. Miller), the Woods Hole Oceanographic Institution (R. Krishfield and J. Ryder), the Institute of Oceanology, Polish Academy of Sciences (A. Beszczynska-Møller), and the officers and crew of the *KV Svalbard* and the *USCGC Healy*. The contributions of the Norwegian Coast Guard and the officers and crew of the *KV Svalbard* (especially G. M. Leinebø, A. Soløy, O. Sletta, and T. Andersen) deserve special mention. After one of the main motors on the *USCGC Healy* failed before the planned recovery of the SIO1, SIO2, and SIO3 moorings, the *KV Svalbard* transited from Norway to the Beaufort Sea in late 2020 and recovered all three moorings. This material is based on work supported by the U.S. Office of Naval Research under Award Nos. N00014-18-1–2149 and N00014-18-1–2698, the Research Council of Norway under Project No. 280531, the European Union Horizon 2020 Programme under Grant Agreement ID No. 727890, and the European Union Horizon Europe Programme, Grant Agreement No. 101094621. Any opinions, findings, and conclusions or recommendations expressed in this publication are those of the authors and do not necessarily reflect the views of the Office of Naval Research. Views and opinions expressed are those of the author(s) only and do not necessarily reflect those of the European Union or the European Research Executive Agency. Neither the European Union nor the granting authority can be held responsible for them.

AUTHOR DECLARATIONS

Conflict of Interest

The authors have no conflicts to disclose.

DATA AVAILABILITY

The data that support the findings of this study are available from the corresponding author upon reasonable request.

APPENDIX: IN SITU SOURCE CHARACTERIZATION

The SIO1 and NERSC1 transceiver moorings recorded their own transmissions. These data were used to evaluate the characteristics (source level, resonant frequency, Q) of the GTI C-BASS M72 acoustic sources, as well as the stability of the source characteristics over the approximately year-long deployments. Because of the relatively shallow source depths (~60 m), the direct and surface-reflected arrivals overlapped significantly at the Hydrophone Modules, given the signal digit length of 8/35 s. A model consisting of two overlapping arrivals was therefore fit to the received signals to extract the source characteristics.

The recordings of the transmitted signal made by the hydrophones on the source moorings SIO1 and NERSC1 were used to estimate the source level, defined as

$$SL = 20\log_{10} p_{rms}, \tag{A1}$$

where $p_{rms} = \sqrt{(1/N)\sum_{i=1}^{N} |p[t_i]|^2}$ is the rms pressure at the transducer averaged over the *m*-sequence transmission. The hydrophones within $\sim$650 m of the source depth were saturated or distorted. At greater depth, the hydrophones record both the direct path arrival and the surface-reflected path arrrival which are of similar magnitude. (As noted in Sec. II, the sources are omnidirectional.) Due to interference between these two arrivals, the recorded signal peak level is not a direct measurement of the transmitted signal source level at the transducer. In order to estimate the transmitted signal source level, the data on the deeper hydrophones were fit with a model of the transducer and the acoustic propagation.

The signal waveform received at a given hydrophone, after both *m*-sequence compression and coherent summation of sequential transmissions, is assumed to be determined by seven parameters: a source amplitude scaling A_{db}, the transducer resonant frequency ω_r, the transducer quality factor Q_r, the source depth z_s, the hydrophone depth z_r, the direct path mean slowness s_D, and the reflected path mean slowness s_R. The surface reflection coefficient R is assumed to be -1 for all transmissions.

Let $\mathbf{x} = [A_{db}, f_r, Q_r, z_s, z_r, s_D, s_R]^T$ be the vector of signal parameters. The data received at a hydrophone, in the frequency domain, is modeled as

$$X(\omega) = S(\omega, \mathbf{x}) + N(\omega), \tag{A2}$$

where $S(\omega, \mathbf{x})$ is the signal and $N(\omega)$ is an additive white Gaussian noise term. Due to the linearity of both the transducer and acoustic propagation, the signal can be expressed as the product of the driving signal Fourier transform S_0, the transducer transfer function H_t, and the acoustic propagation transfer function H_p,

$$S(\omega, \mathbf{x}) = \alpha\, 10^{A_{db}/20} S_0(\omega) H_t(\omega, f_r, Q_r) H_p(\omega, z_s, z_r, s_D, s_R). \tag{A3}$$

The term α is a scalar so that the transducer output peak magnitude is equal to 1 when f_r and Q_r equal their nominal values of 35 Hz and $Q_r = 8.0$.

After *m*-sequence compression, the driving signal is 8 cycles of a sine function at $\omega_c = 2\pi\, 35\,\mathrm{rad\,s^{-1}}$, which has a Fourier transform,

$$S_0(\omega) = -jT\left[\frac{\sin\left(\frac{1}{2}(\omega-\omega_c)T\right)}{\frac{1}{2}(\omega-\omega_c)T} - \frac{\sin\left(\frac{1}{2}(\omega+\omega_c)T\right)}{\frac{1}{2}(\omega+\omega_c)T}\right], \quad \text{(A4)}$$

with $T = 8/35$ s. The transducer is modeled as a damped harmonic oscillator

$$H_t(\omega,\omega_r,Q_r) = \frac{j\omega}{j\omega/\omega_r^2 + 1/(\omega_r Q_r) + 1/(j\omega)}. \quad \text{(A5)}$$

The propagation, corresponding to a point source in an infinite halfspace with a perfectly reflecting surface, has a transfer function

$$H_p(\omega, z_s, z_r, s_D, s_R) = \frac{e^{-j\omega|z_r - z_s|s_D}}{|z_r - z_s|} - \frac{e^{-j\omega|z_r + z_s|s_R}}{|z_r + z_s|}. \quad \text{(A6)}$$

After estimation of the parameter vectors, the estimated transducer output time series $\widehat{h}_{out}(t)$ is the inverse Fourier transform of

$$\widehat{H}_{out}(\omega) = \alpha\, 10^{\widehat{A}_{db}/20} S_0(\omega) H_t\left(\omega, \widehat{f}_r, \widehat{Q}_r\right), \quad \text{(A7)}$$

where $\widehat{(\cdot)}$ denotes the estimated value of the quantity $(\cdot)$. The estimated peak level in decibels is then

$$\widehat{PL} = 20\log_{10} \max_t \left|\widehat{h}_{out}(t)\right|. \quad \text{(A8)}$$

The estimated rms source level in decibels is related to the estimated peak level by

$$\widehat{SL} = \widehat{PL} - PG - C, \quad \text{(A9)}$$

where PG is the signal amplitude processing gain (not the SNR gain), and C is the conversion factor between peak level and rms level. The processing gain that results from the 255-digit m-sequence and the coherent summation of 12 m-sequence periods is 69.7 dB. The conversion factor is 4.1 dB. For a sinusoidal input, the conversion factor between peak and rms level is equal to 3 dB. However, when driving the transducer with an m-sequence, there is a ramp up period after each phase change in the input signal before the transducer reaches steady state. Therefore, the traditional factor of 3 dB for a sinusoidal input overestimates the true rms level. The correct value of 4.1 dB was computed using the transducer model and the known input m-sequence signal.

Bayesian estimation was used to fit the model to the data. The prior uncertainty of the model parameters $\mathbf{x}$ was modeled as a Gaussian random variable. The prior mean $\boldsymbol{\mu}$ used nominal transducer values of $f_r = 35$ Hz, $Q_r = 8$, the source depth and receiver depths estimated from the mooring corrections, and the nominal peak level, which was 191 dB. The WOA 2023 sound speed profile at the mooring latitudes was used to obtain the prior mean for the direct and

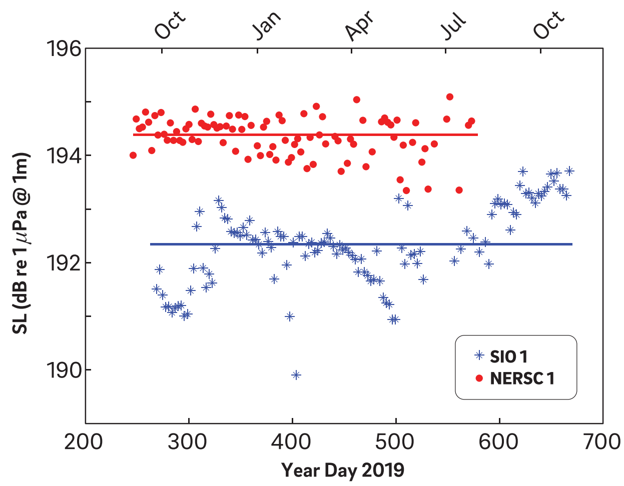

FIG. 19. CAATEX rms source levels for the SIO1 and NERSC1 sources. The variation in the SIO1 source level as a function of year day is thought to be due to a malfunctioning pressure compensation system.

reflected path slowness. The prior covariance $\mathbf{P}_0$ is taken to be diagonal, with standard deviations of 1 m for the source and receiver positions, 5×10^{-6} s/m for the slowness (corresponding to 10 m/s uncertainty in the sound speed), 3 Hz for the transducer resonant frequency, and 1 for the transducer Q−factor. The prior amplitude standard deviation was taken to be 10 decibels. Based on this model, the maximum *a posteriori* estimate of the parameter vector $\mathbf{x}$ minimizes a cost function that measures the model and prior misfit,

$$\hat{\mathbf{x}}_{MAP} = \operatorname{argmin} J(\mathbf{x}), \quad \text{(A10)}$$

where the cost function is

$$J(\mathbf{x}) = \frac{1}{\sigma^2}\|X(\omega) - S(\omega,\mathbf{x})\|^2 + (\mathbf{x}-\boldsymbol{\mu})\boldsymbol{P}_0^{-1}(\mathbf{x}-\boldsymbol{\mu}), \quad \text{(A11)}$$

and σ^2 is the measurement noise spectral density. The noise level corresponds to a signal-to-noise ratio of 15 dB. This minimization was performed with the Gauss–Newton method, an iterative gradient-based optimization algorithm, for the bottom ten receivers of each mooring. The final estimate is the mean estimate over the ten receivers and is shown in Fig. 19 for SIO1 and NERSC1 for all transmissions.

Akins, F. H., Worcester, P. F., Sagen, H., and Dzieciuch, M. A. (**2025**). "Modal group delay estimation for dispersive modes in broadband Arctic tomography," IEEE J. Oceanic Eng. (published online).
APL-UW (**2008**). "Acoustic navigation and communications for high-latitude ocean research," in *ANCHOR Workshop* (Applied Physics Laboratory, University of Washington, Seattle, WA).
Birdsall, T. G., and Metzger, K. (**1986**). "Factor inverse matched filtering," J. Acoust. Soc. Am. **79**, 91–99.
Buck, J. R., Preisig, J. C., and Wage, K. E. (**1998**). "A unified framework for mode filtering and the maximum a posteriori mode filter," J. Acoust. Soc. Am. **103**, 1813–1824.
Colosi, J. A. (**2016**). *Sound Propagation Through the Stochastic Ocean* (Cambridge University Press, Cambridge, UK).

Freitag, L., Ball, K., Partan, J., Koski, P., and Singh, S. (**2015**). "Long range acoustic communications and navigation in the Arctic," in *Proceedings of Oceans 2015 MTS/IEEE*, Washington, DC (October 19–22), pp. 1–5.
Gavrilov, A. N., and Mikhalevsky, P. N. (**2002**). "Recent results of the ACOUS (Arctic Climate Observation using Underwater Sound) Program," Acta Acust. Acust. **88**, 783–791.
Gavrilov, A. N., and Mikhalevsky, P. N. (**2006**). "Low-frequency acoustic propagation loss in the Arctic Ocean: Results of the Arctic climate observations using underwater sound experiment," J. Acoust. Soc. Am. **119**, 3694–3706.
Harris, F. J. (**1978**). "On the use of windows for harmonic analysis with the discrete Fourier transform," Proc. IEEE **66**, 51–83.
Helstrom, C. W. (**1968**). *Statistical Theory of Signal Detection* (Pergamon Press, Oxford, UK), p. 278.
Hermand, J. P., and Roderick, W. I. (**1993**). "Acoustic model-based matched filter processing for fading time-dispersive ocean channels: Theory and experiment," IEEE J. Oceanic Eng. **18**, 447–465.
Howe, B. M., Miksis-Olds, J., Rehm, E., Sagen, H., Worcester, P. F., and Haralabus, G. (**2019**). "Observing the oceans acoustically," Front. Mar. Sci. **6**(426), 426.
IOC, SCOR, and IAPSO (**2010**). *The International Thermodynamic Equation of Seawater – 2010: Calculation and Use of Thermodynamic Properties* (Intergovernmental Oceanographic Commission, Paris, France).
Jakobsson, M., Mohammad, R., Karlsson, M., Salas-Romero, S., Vacek, F., Heinze, F., Bringensparr, C., Castro, C. F., Johnson, P., Kinney, J., Cardigos, S., Bogonko, M., Accettella, D., Amblas, D., An, L., Bohan, A., Brandt, A., Bünz, S., Canals, M., Casamor, J. L., Coakley, B., Cornish, N., Danielson, S., Demarte, M., Di Franco, D., Dickson, M.-L., Dorschel, B., Dowdeswell, J. A., Dreutter, S., Fremand, A. C., Hall, J. K., Hally, B., Holland, D., Hong, J. K., Ivaldi, R., Knutz, P. C., Krawczyk, D. W., Kristofferson, Y., Lastras, G., Leck, C., Lucchi, R. G., Masetti, G., Morlighem, M., Muchowski, J., Nielsen, T., Noormets, R., Plaza-Faverola, A., Prescott, M. M., Purser, A., Rasmussen, T. L., Rebesco, M., Rignot, E., Rysgaard, S., Silyakova, A., Snoeijs-Leijonmalm, P., Sørensen, A., Straneo, F., Sutherland, D. A., Tate, A. J., Travaglini, P., Trenholm, N., van Wijk, E., Wallace, L., Willis, J. K., Wood, M., Zimmermann, M., Zinglersen, K. B., and Mayer, L. (**2024**). "The international bathymetric chart of the Arctic Ocean version 5.0," Sci. Data **11**, 1420.
Krishfield, R., Toole, J., Proshutinsky, A., and Timmermans, M. L. (**2008**). "Automated ice-tethered profilers for seawater observations under pack ice in all seasons," J. Atmos. Oceanic Technol. **25**, 2091–2105.
Krishfield, R. A., Proshutinsky, A., Tateyama, K., Williams, W. J., Carmack, E. C., McLaughlin, F. A., and Timmermans, M. L. (**2014**). "Deterioration of perennial sea ice in the Beaufort Gyre from 2003 to 2012 and its impact on the oceanic freshwater cycle," J. Geophys. Res. Oceans **119**, 1271–1305, https://doi.org/10.1002/2013jc008999.
Kucukosmanoglu, M., Colosi, J. A., Worcester, P. F., Dzieciuch, M. A., Sagen, H., Duda, T. F., Zhang, W. G., Miller, C. W., and Richards, E. L. (**2023**). "Observations of the space/time scales of Beaufort sea acoustic duct variability and their impact on transmission loss via the mode interaction parameter," J. Acoust. Soc. Am. **153**, 2659–2676.
Locarnini, R. A., Mishonov, A. V., Baranova, O. K., Reagan, J. R., Boyer, T. P., Seidov, D., Wang, Z., Garcia, H. E., Bouchard, C., Cross, S. L., Paver, C. R., and Dukhovskoy, D. (**2024**). *World Ocean Atlas 2023, Volume 1: Temperature*, edited by A. Mishonov (NOAA National Centers for Environmental Information, Asheville, NC).
McLaughlin, F., Carmack, E., Proshutinsky, A., Krishfield, R. A., Guay, C., Yamamoto-Kawai, M., Jackson, J. M., and Williams, B. (**2011**). "The rapid response of the Canada Basin to climate forcing: From bellwether to alarm bells," Oceanography **24**, 146–159.
Meier, W. N., and Stroeve, J. (**2022**). "An updated assessment of the changing Arctic sea ice cover," Oceanography **35**, 10–19.
Mikhalevsky, P. N., Baggeroer, A. B., Gavrilov, A., and Slavinsky, M. (**1995**). "Experiment tests use of acoustics to monitor temperature and ice in Arctic Ocean," EoS. Trans. **76**, 265–269.
Mikhalevsky, P. N., and Gavrilov, A. N. (**2001**). "Acoustic thermometry in the Arctic Ocean," Polar Res. **20**, 185–192.
Mikhalevsky, P. N., Gavrilov, A. N., and Baggeroer, A. B. (**1999**). "The Transarctic Acoustic Propagation Experiment and climate monitoring in the Arctic," IEEE J. Oceanic Eng. **24**, 183–201.
Mikhalevsky, P. N., Gavrilov, A. N., Moustafa, M. S., and Sperry, B. (**2001**). "Arctic Ocean warming: Submarine and acoustic measurements," in *Proceedings of OCEANS 2001 MTS/IEEE Conference Proceedings*, pp. 1523–1528.
Mikhalevsky, P. N., Sagen, H., Worcester, P. F., Baggeroer, A. B., Orcutt, J., Moore, S. E., Lee, C. M., Vigness-Raposa, K. J., Freitag, L., Arrott, M., Atakan, K., Beszczynska-Möller, A., Duda, T. F., Dushaw, B. D., Gascard, J. C., Gavrilov, A. N., Keers, H., Morozov, A. K., Munk, W. H., Rixen, M., Sandven, S., Skarsoulis, E., Stafford, K. M., Vernon, F., and Yuen, M. Y. (**2015**). "Multipurpose acoustic networks in the Integrated Arctic Ocean Observing System," Arctic **68**, 11–27.
Munk, W., Worcester, P., and Wunsch, C. (**1995**). *Ocean Acoustic Tomography* (Cambridge University Press, Cambridge, UK).
Polyakov, I. V., Alkire, M. B., Bluhm, B. A., Brown, K. A., Carmack, E. C., Chierici, M., Danielson, S. L., Ellingsen, I., Ershova, E. A., Gårdfeldt, K., Ingvaldsen, R. B., Pnyushkov, A. V., Slagstad, D., and Wassmann, P. (**2020**). "Borealization of the Arctic Ocean in response to anomalous advection from Sub-Arctic seas," Front. Mar. Sci. **7**(491), 491.
Polyakov, I. V., Pnyushkov, A. V., and Timokhov, L. A. (**2012**). "Warming of the intermediate Atlantic water of the Arctic Ocean in the 2000s," J. Clim. **25**, 8362–8370.
Rantanen, M., Karpechko, A. Y., Lipponen, A., Nordling, K., Hyvärinen, O., Ruosteenoja, K., Vihma, T., and Laaksonen, A. (**2022**). "The Arctic has warmed nearly four times faster than the globe since 1979," Commun. Earth Environ. **3**(168), 168.
Reagan, J. R., Boyer, T. P., García, H. E., Locarnini, R. A., Baranova, O. K., Bouchard, C., Cross, S. L., Mishonov, A. V., Paver, C. R., Seidov, D., Wang, Z., and Dukhovskoy, D. (**2024a**). *World Ocean Atlas 2023* (NOAA National Centers for Environmental Information, Asheville, NC).
Reagan, J. R., Seidov, D., Wang, Z., Dukhovskoy, D., Boyer, T. P., Locarnini, R. A., Baranova, O. K., Mishonov, A. V., Garcia, H. E., Bouchard, C., Cross, S. L., and Paver, C. R. (**2024b**). *World Ocean Atlas 2023, Volume 2: Salinity*, edited by A. Mishonov (NOAA National Centers for Environmental Information, Asheville, NC).
Timmermans, M.-L., Proshutinsky, A., Golubeva, E., Jackson, J. M., Krishfield, R., McCall, M., Platov, G., Toole, J., Williams, W., Kikuchi, T., and Nishino, S. (**2014**). "Mechanisms of Pacific Summer Water variability in the Arctic's Central Canada basin," J. Geophys. Res. Oceans **119**, 7523–7548, https://doi.org/10.1002/2014jc010273.
Wage, K. E., Baggeroer, A. B., and Preisig, J. C. (**2003**). "Modal analysis of broadband acoustic receptions at 3515-km range in the North Pacific using short-time Fourier techniques," J. Acoust. Soc. Am. **113**, 801–817.
Worcester, P. F., and Ballard, M. S. (**2020**). "Ocean acoustics in the changing Arctic," Phys. Today **73**(12), 44–49.
Worcester, P. F., Carey, S., Dzieciuch, M. A., Green, L. L., Horwitt, D., Lemire, J. C., and Norenberg, M. (**2009**). "Distributed vertical line array (DVLA) acoustic receiver," in *Proceedings of the 3rd International Conference on Underwater Acoustic Measurements: Technologies and Results*, edited by J. S. Papadakis, and L. Bjørnø (Foundation for Research and Technology Hellas, Nafplion, Greece), pp. 113–118.
Worcester, P. F., Dzieciuch, M. A., Colosi, J. A., Krishfield, R. A., Vazquez, H. J., and Kemp, J. N. (**2024**). "Transmission loss of surface-reflected ray arrivals underneath seasonally varying sea ice in the Canada Basin during 2016–2017," J. Acoust. Soc. Am. **156**, 4181–4192.
Worcester, P. F., Dzieciuch, M. A., Mercer, J. A., Andrew, R. K., Dushaw, B. D., Baggeroer, A. B., Heaney, K. D., D'Spain, G. L., Colosi, J. A., Stephen, R. A., Kemp, J. N., Howe, B. M., Van Uffelen, L. J., and Wage, K. E. (**2013**). "The North Pacific Acoustic Laboratory deep-water acoustic propagation experiments in the Philippine Sea," J. Acoust. Soc. Am. **134**, 3359–3375.